IOP PUBLISHING and INTERNATIONAL ATOMIC ENERGY AGENCY NUCLEAR FUSION
Nucl. Fusion **49** (2009) 095003 (9pp) doi:10.1088/0029-5515/49/9/095003

Self-consistent analysis of the effect of runaway electrons on plasma facing components in ITER

V. Sizyuk and A. Hassanein

Purdue University, West Lafayette, IN 47907, USA

E-mail: vsizyuk@purdue.edu (V. Sizyuk) and hassanein@purdue.edu (A. Hassanein)

Received 21 January 2009, in final form 25 June 2009
Published 13 August 2009
Online at stacks.iop.org/NF/49/095003

Abstract
Physical and computational models are developed, used and benchmarked for studying the response of ITER tokamak plasma facing components to runaway electron impact following a plasma disruption. The energy deposition, temperature evolution and material melting thickness are calculated for a wide range of runaway electron parameters, namely, electron kinetic energy, magnetic field, energy partition ratio (along and across magnetic field direction) impact duration, and wall material composition. It is shown that the electron energy partition ratio will have a significant effect on the wall heat load with melting of the first wall with beryllium armor possible. If tungsten armor is used instead, the surface of the mockup is overheated and melted for all ranges of studied parameters of the runaway electrons. Using an insert of a thin layer of a high-Z material inside the beryllium armor can mitigate the heat load in the armor and heat sink structure.

PACS numbers: 52.40.Hf, 52.55.Fa, 52.55.Pi, 52.65.Pp

1. Introduction

The toroidal electric field in tokamak plasma devices gives rise to the runaway electron phenomenon during the current phase of a plasma disruption. Due to the decrease in the Coulomb collision frequency with increasing energy, electrons with energies larger than a critical threshold value are continuously accelerated by the electric field. The accelerated electrons excite waves due to the anomalous Doppler effect, i.e. a gyrating electron is similar to a flying oscillator [1]. In its coordinate system, a wave with phase velocity smaller than the electron phase velocity seems like a wave with ‘negative’ energy. Therefore, the runaway electron can excite a wave, and increase its lateral energy and decrease its longitudinal velocity. Because of the generation of such fan type instability, the tokamak plasma initiates an oscillation burst with high-energy electron emission [2, 3]. The runaway electron phenomena were discussed at the 6th IAEA Technical Committee Meeting (2000) where its status was changed from an innocuous phenomenon, mainly used to probe magnetic turbulence, to a serious threat to the ITER (or any future large tokamak) first wall [4]. The effect of the runaway electrons impinging at the vessel walls is strongly dependent on the energy gained in the tokamak toroidal electric field. To date, a number of experimental [2, 3, 5–10] and theoretical [11–14] investigations exist to predict the main parameters of the runaway electrons. These studies analysed the energy of electrons, energy density of the runaway electron impact and duration of the electron impact. Several numerical simulations were carried out using realistic tokamak wall geometries and runaway electron impact parameters [15–20] and showed surface melting of wall armor material of up to several millimetres depth.

The aim of this paper is to develop integrated modelling to predict the behaviour of the ITER first wall geometry [19] for a wide range of runaway electron parameters using the integrated self-consistent high energy interaction with general heterogeneous target systems (HEIGHTS) computer package [21–23]. This package is capable of predicting the details of internal damage of the first wall assembly in full 3D. The HEIGHTS package is then used to develop a safe design configuration to prevent surface and internal structural melting.

2. Mathematical and physical model

The HEIGHTS integrated model has been developed as an instrument for the simulation and optimization of the interaction processes during the intense energy deposition of various energy sources such as plasma, laser and particle beams

0029-5515/09/095003+09$30.00

incident on target materials. Recently, HEIGHTS investigated in detail the effect of plasma instabilities including VDEs, ELMs and disruptions on plasma facing components (PFCs) of a tokamak reactor [21, 22]. The integrated model combines four main parts: energy deposition, target hydrodynamic evolution, radiation transport and energy dissipation (with both heat conduction and magnetic diffusion). The energy deposition model was upgraded in HEIGHTS for the case of runaway electron deposition by taking into account the various interaction mechanisms of beam electrons with surface target atoms. For pair collisions, the incident particle is assumed to interact simultaneously with only one particle of the target (nucleus or electron). This interaction occurs at one point and instantly. Our Monte Carlo model is based on this principle and assumes that energetic particles are remote from each other by a distance larger than the Coulomb shielding in the target. Because runaway electrons have initially relativistic energy, we included in our relativistic Monte Carlo model six main processes [24–28]: (1) electron–electron scattering; (2) electron–nuclear scattering; (3) Bremsstrahlung; (4) photoabsorption; (5) Compton absorption and (6) Auger relaxation. The effect of electron-positron pair production is not included as a secondary process (after photon generation via incident electron interaction). This process is important for energy deposition of very high photons energies [29].

Our Monte Carlo model is based on the pair collisions approximation 30. The transport of electrons is therefore, dominated by the long-range Coulomb force. This results in large numbers of small interactions. For example, an electron in aluminium slowing down from 500 to 63 keV will undergo about 10^5 individual interactions. Therefore, it is not practical to try to simulate every interaction, i.e. a single-collision Monte Carlo approach to electron transport is infeasible for many situations of practical interest. On the other hand, the low momentum transfer events that give rise to large cross-section values do not result in large fluctuations in energy deposition. For this reason, they are lumped together and treated in a continuous manner. The energy losses are due to soft interactions with the atomic electrons (excitation and ionization loss). The changes in electron direction are mostly due to multiple Coulomb scattering from the nucleus, with some contribution from soft electron scattering. Due to limited computer power, it is not possible to take into account all interactions of incident particles with every target particle. To obtain reasonable accuracy, the scattering result of a large enough number of separate collisions can be expanded on all target interactions (see, for example, the TIGER code [31]). However, most interactions do not separately have a critical effect on the incident particle initial energy or direction of motion. The combined contribution of all small interactions is important, however, and comparable to the interaction of close scattering events. Again, modelling of many small interactions as separate events will significantly decrease calculation efficiency. To overcome this problem, we combined all interactions into two groups: close collisions and distant collisions as commonly used in other Monte Carlo codes. The criterion for the grouping is the energy that is transmitted to the recoiled particle. In this model, all interactions where incident particles lose $<1\%$ of their initial energy are defined as distant. The distant interactions contribution (energy and direction) is accumulated on a trajectory between two neighbour close collisions and added at the end of the trajectory. The exact border between close and distant collisions is varied and depends on computer resources and needed accuracy. The developed HEIGHTS Monte Carlo model makes use of the low energy transfer grouping method [32].

The atomic electrons of the interacting medium are considered free and at rest with respect to the incident electrons with kinetic energy higher than 1 keV. This assumption is fairly accurate because the characteristic velocity of the atomic electrons is negligible compared with the high velocity of the incident runaway electrons. In the laboratory coordinate system the differential cross-section of energy transfer to the atomic electron $\mathrm{d}\sigma_{\mathrm{ee}}$ has the form [24]

$$\frac{\mathrm{d}\sigma_{\mathrm{ee}}}{\mathrm{d}\Delta} = \frac{2\pi r_{\mathrm{e}}^2}{\gamma^2 - 1}\left\{\frac{(\gamma-1)^2\gamma^2}{\Delta^2(\gamma-1-\Delta)^2} - \frac{2\gamma^2+2\gamma-1}{\Delta(\gamma-1-\Delta)} + 1\right\}, \tag{1}$$

where $\Delta = T/m_{\mathrm{e}}c^2$ is the transferred energy from the incident electron to the target electron reduced to the electron self-energy $m_{\mathrm{e}}c^2$; $\gamma = (E + m_{\mathrm{e}}c^2)/m_{\mathrm{e}}c^2$ is the reduced energy of incident electron before scattering; $r_{\mathrm{e}} = e^2/m_{\mathrm{e}}c^2$ is the classical electron radius; m_{e} is the electron mass; e is the electron charge and c is the speed of light. (Here and below we used the Gaussian unit system.) Assuming Δ^* is the threshold energy between the close and distant collisions, the integration of equation (1) from the interval of energy Δ^* to the possible maximum transferred energy $\Delta_{\max} = 0.5(\gamma - 1)$ gives the expression for the close collisions total cross-section in [1/cm]:

$$\sigma_{\mathrm{ee}} = \frac{2\pi e^4 z N}{(\gamma^2-1)\, m_{\mathrm{e}}^2c^4}\left\{\frac{\gamma-1}{2} - \frac{\gamma^2}{\gamma-1-\Delta^*} - \frac{\gamma^2}{\Delta^*} + \frac{2\gamma-1}{\gamma-1}\ln\left(\frac{\gamma-1-\Delta^*}{\Delta^*}\right) + \Delta^*\right\}, \tag{2}$$

where z is the nuclear charge of target atoms and N is the number density of target atoms.

The energy loss per unit length x in distant collisions is obtained by the integration of equation (1) in the range up to Δ^*. Performing this integration, one obtains

$$\left(\frac{\mathrm{d}E}{\mathrm{d}x}\right)_{\mathrm{ee}} = \frac{2\pi z\gamma^2Ne^4}{(\gamma^2-1)m_{\mathrm{e}}c^2}\left\{\ln\left[\frac{(\gamma^2-1)\Delta^* m_{\mathrm{e}}^2c^4}{I_0^2}\right] - \left[\frac{2}{\gamma} - \frac{1}{\gamma^2} + 1\right]\ln\left[\frac{1}{1-\frac{\Delta^*}{2(\gamma-1)}}\right] + \frac{1}{1-\frac{\Delta^*}{2(\gamma-1)}} + \frac{1}{\gamma^2} + \frac{\Delta^{*2}}{8\gamma^2} - 2\right\}. \tag{3}$$

Here I_0 is the average ionization potential. This parameter used in the Bethe theory is formally defined by $z\ln I_0 = \sum_n f_n \ln E_n$, where E_n and f_n are the possible electronic energy transitions and corresponding dipole oscillator strengths for the medium atoms [27, 28].

Elastic nuclear scattering processes are the main contribution to the deflection of electrons. Energy loss in these collisions per unit length is vanishingly small in comparison with electron–electron interactions and can be neglected. The close collisions cross-section is obtained by integration per Rutherford representation [24]

$$\sigma_{\mathrm{en}} = \pi N\left(\frac{ze^2}{2E}\right)^2\frac{1+\cos\theta^*}{1-\cos\theta^*}, \tag{4}$$

where θ^* is the deviation angle corresponding to threshold energy T^* between close and distant collisions. The kinematic relationship for the deviation angle and transferred energy is taken into account as

$$T = 4\frac{m_e m_n}{(m_e + m_n)^2} E \sin^2\frac{\theta}{2} \tag{5}$$

with m_n as the target particle mass.

The bremsstrahlung process was modelled following the Bethe–Heitler relativistic theory [24, 33, 34] with the differential cross-section $d\sigma_{br}$ given by

$$\frac{d\sigma_{br}}{dE_{ph}d\Omega_{ph}d\Omega_e} = \frac{z^2\alpha e^4}{4\pi^2}\frac{p'_e m_e^2 c^2}{p_e p_n^4 E_{ph}}\left[\frac{p_n^2}{\eta\eta' m_e^2 c^2}(2E_{et}^2 + 2E'^2_{et} - p_n^2 c^2) + p_n^2 c^2\left(\frac{1}{\eta} - \frac{1}{\eta'}\right)^2 - 4\left(\frac{E_{et}}{\eta'} - \frac{E'_{et}}{\eta}\right)^2 + \frac{2E_{ph}p_n^2}{m_e^2 c^2}\left(\frac{1}{\eta'} - \frac{1}{\eta}\right) - \frac{2E_{ph}^2}{m_e^2 c^4}\left(\frac{\eta'}{\eta} + \frac{\eta}{\eta'}\right)\right], \tag{6}$$

where indexes ph, e, n corresponds to photon, electron and nucleus; E_{ph} is the generated photon energy; Ω is the solid angle of particle after collision; α is the fine structure constant; p, p' are particle momentums before and after scattering; $\eta = E_{et} - \vec{n}\vec{p}_e c$, $\eta' = E'_{et} - \vec{n}\vec{p}'_e c$ are reduced energies; $E_{et} = E_e + m_e c^2$, $E'_{et} = E'_e + m_e c^2$ are total electron energy before and after collision and the vector $\vec{n}$ is determined through wave vector $\vec{k}$ as $\vec{n} = \vec{k}/\omega$. Detailed derivation of equation (6) Monte Carlo modelling can be found in [25, 26].

The photoabsorption cross-section depends essentially on the charge of the medium nuclei and the photon energy. Increasing the nucleus charge multiplies the absorption as z^n, where n is usually in the range from 4 up to 5 depending on the photon energy. For low energies (<0.2 MeV) the absorption cross-section is proportional to $1/E_{ph}^3$. For high energies (>0.5 MeV) the cross-section is proportional to $1/E_{ph}$. In the case of high-energy photons the maximal absorption occurs at the K-shell of the target atoms. The differential cross-section of photoabsorption is then written in the following form [24]

$$\frac{d\sigma_{ph}}{d\Omega} = \sigma_n(E_{ph})\sin^2\theta\cos\varphi(1 + 4\beta\cos\theta), \tag{7}$$

where $d\Omega$ is the solid angle of the ejected photoelectron; $\sigma_n(E_{ph})$ is the cross-section of photoabsorption at the corresponding shell; θ, φ are the polar and azimuthal angles; $\beta = v/c$ and v is the photoelectron velocity. The σ_n is determined from the result of quantum mechanical calculations in accordance with the Hartree–Fock–Slater model [27, 28]. We assumed also that the Auger photons generated by relaxation of electron shells are absorbed within the same calculation cell due to their low energy.

When the resultant photon energy is higher than the average ionization potential of the medium atoms Compton scattering is the predominant interaction process. In Compton scattering a photon interacting with an atomic electron changes its direction and transfers part of its energy to the electron. This process dominates in the energy range 1–50 MeV for elements with low and mean atomic numbers [29]. We modelled the Compton processes following the Klein–Nishina–Tamm theory, where the differential cross section $d\sigma_{com}$ can be expressed as

$$\frac{d\sigma_{com}}{dE'_{ph}} = \frac{\pi r_e^2 m_e c^2}{E_{ph}^2}\left[\frac{E_{ph}}{E'_{ph}} + \frac{E'_{ph}}{E_{ph}} + \left(\frac{m_e c^2}{E'_{ph}} - \frac{m_e c^2}{E_{ph}}\right)^2 - 2m_e c^2\left(\frac{1}{E'_{ph}} - \frac{1}{E_{ph}}\right)\right], \tag{8}$$

which was integrated to obtain total cross-section of scattering in [1/cm]

$$\sigma_{com} = 2\pi r_e^2\frac{N}{x}\left[\left(1 - \frac{4}{x} - \frac{8}{x^2}\right)\ln(1+x) + \frac{1}{2} + \frac{8}{x} - \frac{1}{2(1+x)^2}\right], \tag{9}$$

Here $x = 2E_{ph}/m_e c^2$ is the reduced energy of the photon.

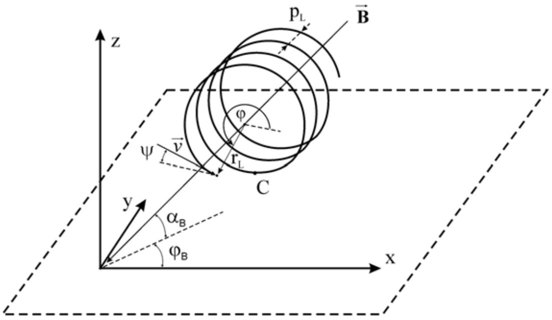

Figure 1. Incident angle ψ of charged particle depends on Larmor radius r_L, spiral pitch p_L, azimuthal particle angle φ and magnetic field incline α_B. The ψ angle is equal to α_B in the case of $\vec{v}||\vec{B}$.

The processes described above were modelled in three-dimensional space using the Neumann method [35]. As we noted, the developed model is related to the small energy transfer grouping scheme [36] most advanced for the construction of branching trajectories. Collisions that transfer large energy are simulated in HEIGHTS as in the model of catastrophic collisions. Collisions with low energy transfer are summed. The length of 'free path' steps between close interactions is sampled randomly by using the derived total macroscopic cross-sections of each process. Along these steps, the electron is assumed to follow a spiral line, and the multiple scattering is accounted for by changing the electron direction at the end of the step. Equation of motion for charged particles in magnetic field is given in [37]. Most of previously published work [15–19] consider the initial runaway electron beam as parallel to the magnetic field. This is done to minimize computer time. However, runaway electrons should have a significant perpendicular to magnetic field component of the velocity as in [2, 3, 5, 12] and should arrive at the first wall surface in a spiral fashion. As shown in figure 1, the incident angle ψ of particle depends on the Larmor radius, on the spiral pitch, and on the magnetic field direction. Our initial calculations showed that the incident angle of the runaway electrons is very important for the target energy deposition because the mean free path of electrons in matter is much shorter since the Larmor radius, and the photons (secondary particles) motion is independent of the magnetic field. Unfortunately, direct analytical solution does not exist

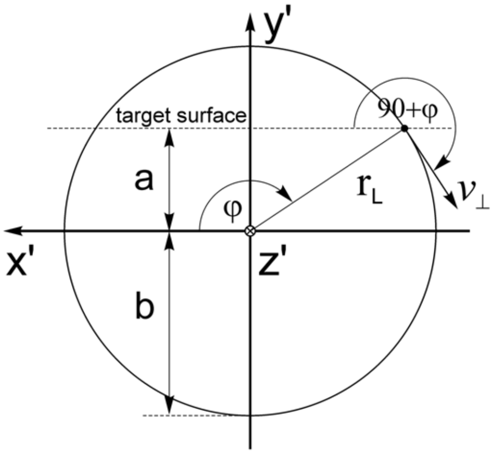

Figure 2. Schematic of the incident electron impact angle.

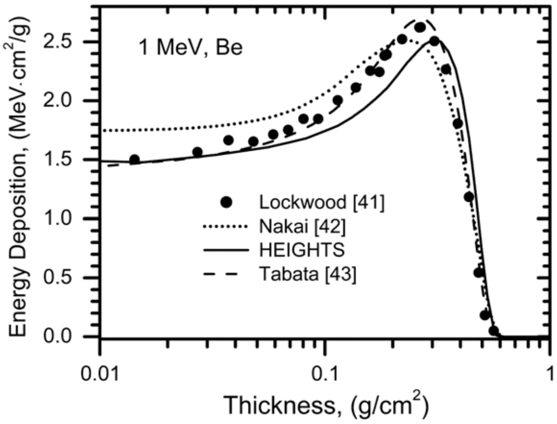

Figure 3. Energy deposition of 1 MeV electrons in beryllium.

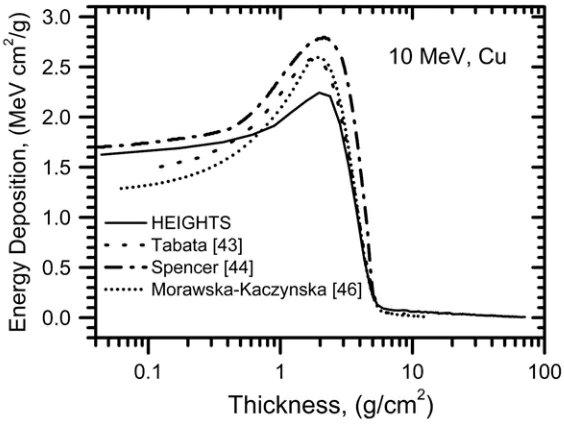

Figure 4. Energy deposition of 10 MeV electrons in copper.

for calculation of the target surface incident angle of a spiral moving particle.

We therefore developed a Monte Carlo algorithm of the electron incident angle sampled at the moment of touching the target surface. Initial parameters are Larmor radius r_L, Larmor spiral pitch p_L and magnetic field incident angle α_B. The incident angle is sampled in coordinate system $S'(x', y', z')$ where one axis (z') is parallel to the magnetic field and the second axis (x') is located on the target surface to limit the transformation in the lab coordinates with only two Euler angles [37]. Figure 2 schematically shows the calculation of the transverse component of runaway electron velocity in the coordinate system S'. The maximum immersion depth of spiral $c = a + b$ can then be calculated as

$$c = p_L \mathrm{abs}\left[\mathrm{tg}\left(\frac{\pi}{2} - \alpha_B\right)\right]. \qquad (10)$$

Therefore, the azimuthal angle φ can be sampled as

$$\sin\varphi = \frac{\xi p_L \mathrm{abs}\left[\mathrm{tg}\left(\frac{\pi}{2} - \alpha_B\right)\right] - r_L}{r_L}, \qquad (11)$$

where ξ is a random number in [0, 1] range. The sampled direction is recalculated into the lab system $S(x, y, z)$ with the Euler transformation [37].

3. Validation and benchmarking

We are interested in benchmarking tests and comparisons that verify the new energy deposition model from fast electrons in first wall materials, since the heat conduction part of the HEIGHTS package is well benchmarked [38–40]. The energy deposition distribution in the standard case of semi-infinite absorbers irradiated by plane-parallel electron beams was chosen for this comparison. We present sample benchmarking calculations using published data. The energy deposition in beryllium for 1 MeV runaway electron deposition is shown in figure 3 for normal beam incidence. The experimental data of Lockwood *et al* [41] and Nakai [42], and theoretical calculations of Tabata [43] are included in this comparison. The Lockwood data are reproduced from the Tabata paper. Our calculations of the integrals of these curves give values of 963 keV for the Lockwood experiment and 996 keV for the Nakai experiment. The Tabata calculations give 979 keV, and the HEIGHTS value is 998 keV, therefore showing good agreement. Figure 4 shows the energy deposition curves for 10 MeV electrons in copper. The comparison is made with results of Tabata [43], Spencer [44] (taken from [45]), and Morawska-Kaczynska [46]. The integral has value 9.58 MeV for the HEIGHTS model, 8.60 MeV for Tabata calculations and 8.61 MeV for [46]. The integral value of 10.36 MeV from the Spencer theory is of concern in our opinion and may have included incorrect data reproduced in [45] from another source.

To further compare our integrated model, we simulated the case of energy deposition of a 10 MeV electron beam with density of 50 MJ m^{-2} and pulse duration of 0.1 s into the tokamak first wall geometry number 1 presented in [19, 20]. The temperature distribution and melted layer (grey) are shown in figure 5 in an equivalent scale to the published data [19]. The value of the toroidal magnetic field was 8 T (at the inboard wall). The reflected particles scattered from the target surface were also taken into account in our calculations. The HEIGHTS-computed molten beryllium thickness was 2.1 mm in comparison with a value of 2.5 mm in [19]. The noticeable difference in temperature on the top and bottom borders of the temperature field in figure 5(*b*) [19] can be explained in terms of using the outermost location of the module element in the computational domain. We modelled the runaway electron impact assuming a periodic mockup structure. This can be

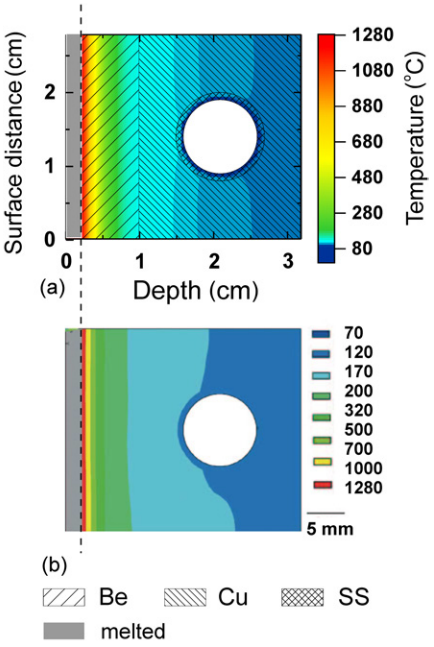

Figure 5. Temperature pattern and melted layer (grey) after energy deposition by 10 MeV electrons (deposition time, 0.1 s; incidence angle, 1°): (*a*) HEIGHTS calculations; (*b*) Maddaluno *et al* [19, 20].

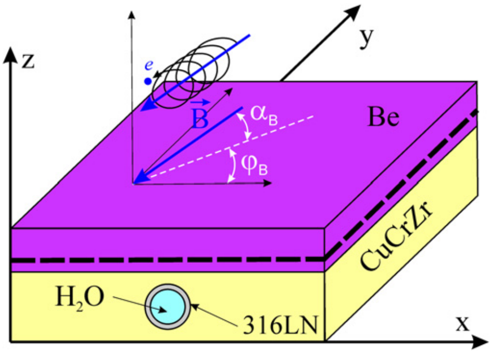

Figure 6. Schematic of first wall geometry and configuration.

done because the beam toroidal length is estimated as 40 cm [19] and the mockup period is 2.8 cm in this direction.

The presented figures above show excellent agreement of HEIGHTS calculations with the published experimental data and numerical simulation. HEIGHTS can therefore be used with reasonable confidence to explore complicated geometry and design optimization for safe operation and mitigation of runaway electron effects.

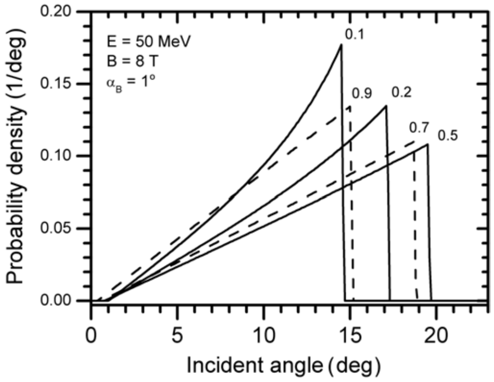

Figure 7. Runaway electron incident angle distributions for various energy ratios. Electron energy, 50 MeV; magnetic field, 8 T and magnetic field inclined angle, 1°.

4. PFC setup and geometry

The geometry 1 given in [19] was used as the basic model for our simulations (see figure 6). Thickness of armor material (Be or W) was assumed 10 mm. The heat sink thickness (CuCrZr alloy) was taken as 22 mm. Stainless steel (316LN) tubes had an internal diameter of 10 mm and an external one of 12 mm, pitch between neighbouring tubes was 28 mm. Coolant tubes were located at the half-thickness of the heat sink. As in [19], we oriented the X-, Y- and Z-axis into the toroidal the poloidal and the radial direction, respectively. The thermal contacts between different materials are considered to be perfect. The thick dashed line in figure 6 represents the location of a prospective additional adsorption layer to mitigate the effect of runaway electrons (see simulation results section below). The magnetic field B in the three-dimensional modelling space had two directional angles: incident angle α_B and azimuth angle φ_B. Water was assumed to be the coolant.

5. Simulation results

As discussed above, the incident angle of electrons into target depends on the Larmor spiral parameters and magnetic field direction. The Larmor radius and spiral pitch are determined from the ratio of the electron kinetic energy across the magnetic field direction and the total particle kinetic energy $E_\perp/E$. Thereafter, using the term energy ratio we mean the $E_\perp/E$ ratio. Because of such complex influence, the actual incident angles of runaway electrons can be significantly different from the initial magnetic field inclination α_B that used in most present calculations. We generated the incident angle distributions for the benchmark case of magnetic field inclination angle of $\alpha_B = 1°$ as shown in figure 7. The curves indicate that the true incident angle has a nonlinear dependence on the energy ratio.

Figure 8 shows the effect of the nonlinearity in molten layer thickness at the minimum and maximum energy ratio values. These calculations were carried out for 50 MeV incident electrons energy, magnetic field inclined of 1° to target surface and impact duration of 0.01 s. The armor material was beryllium. The calculations below show different design cases for ITER assuming a total energy density of 50 MJ m^{-2}, magnetic field value of 8 T (inboard wall) and initial temperature of all materials to be 100 °C. The runaway electron parameters used in this study were taken from those values predicted for ITER and future tokamak devices [3, 19]. As shown in figure 8, the minimum molten layer thickness corresponds to the widely considered case of the electrons directed strongly along the magnetic field [15–19]. Figure 8(*b*) shows the maximum temperature in Be and Cu materials as a function of energy ratio. The case where all incident electrons are parallel to the magnetic field (zero energy ratio) gives the lowest thickness of the overheated layer. A runaway electrons

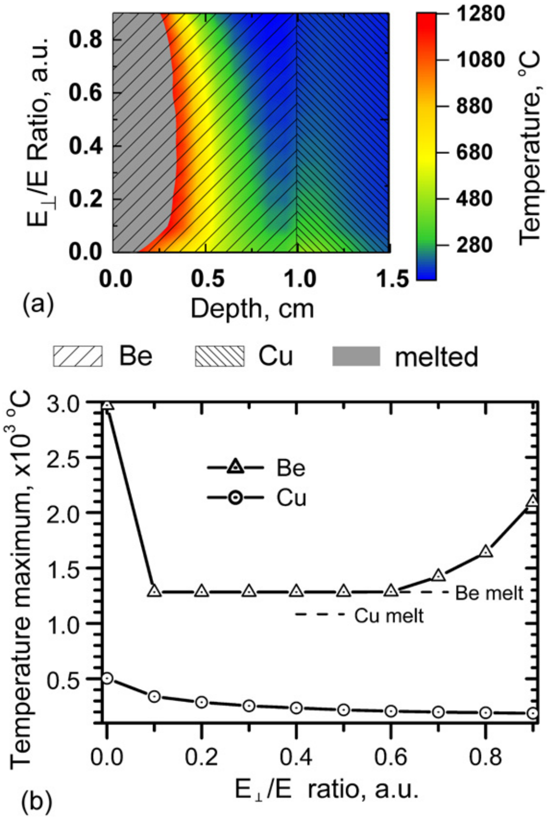

Figure 8. Thermal response as a function of the transverse part of kinetic energy for Be armor directly at the normal axis above cooling tube. Electron energy, 50 MeV; magnetic field, angle, 1° and impact duration, 0.01 s: (*a*) temperature and melting layer (grey) of target; (*b*) maximum temperature of material.

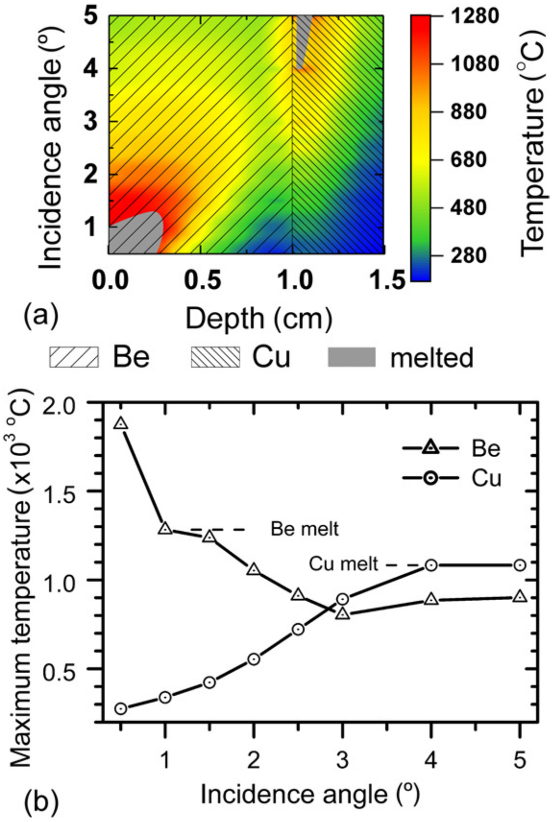

Figure 9. Thermal response as a function of the magnetic field incidence angle for Be armor directly at the normal axis above cooling tube. Electron energy, 50 MeV; energy ratio, 0.1 and impact duration, 0.01 s: (*a*) temperature and melting layer (grey) of target; (*b*) maximum temperature of material.

energy ratio of 0.1 gives more than twice the molten layer thickness than the parallel case.

The magnetic field incident angle variation adds another peculiarity to the first wall damage response. Increasing the magnetic field angle to 4° and larger, the runaway electron energy can be deposited deep into the heat sink copper through the external beryllium armor layer (see figure 9). HEIGHTS modelling shows that for the ratio $E_{\perp}/E = 0.1$, electron energy of 50 MeV and impact duration of 0.01 s, a melting depth of copper of up to 0.86 mm is developed in the 5° case. The beryllium armor, was not melted; however, this permits more electron heat flow to deeper layers. Therefore, magnetic field angles larger than 4° are potentially dangerous for the first wall since it can result in melting of the structure that is harder to repair compared with the armor surface materials. Figure 9 shows such effect of melting of the copper heat sink for the higher energy case of 50 MeV electrons.

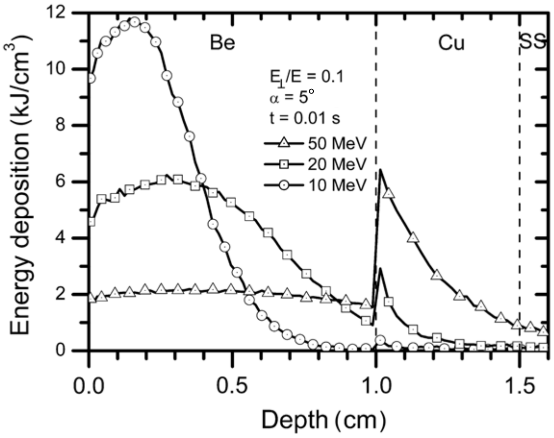

Figure 10. Spatial dependence of the electron energy deposition as a function of incident energy for the Be/Cu/SS structure at the normal axis (magnetic field angle, 5°; energy ratio, 0.1 and impact duration, 0.01 s).

The extent of the wall thermal evolution is strongly dependent on the electron energy deposition profile. Figure 10 shows the spatial distribution of electron energy deposition for Be, Cu and SS composite structure for different incident energies. Energetic electrons penetrate deeper inside the structure and can deposit significant fraction of its energy at the coolant tubes. Figure 11 shows the effect of the kinetic energy of runaway electrons on copper thermal response and melting. The temperature profile is calculated for different initial total energies of the electrons assuming a magnetic field angle of 5°, an energy ratio of 0.1 and impact duration of 0.01 s. As shown, copper melting takes place for incoming electrons energy of 35 MeV or higher. Figure 11(*b*) shows the variation of the maximum material temperature and the melted zones as a function of incident total electron energy. The beryllium armor reaches a maximum temperature for electron energies near 40 MeV. This maximum corresponds to the beryllium–copper border, i.e. armor heating by thermal conduction.

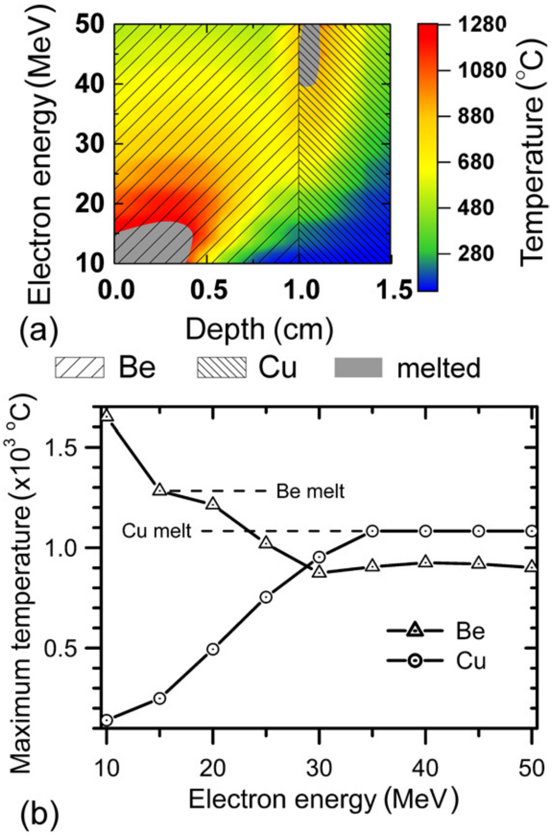

Figure 11. Thermal response as a function of the electron incident energy for Be armor directly at the normal axis above the coolant tube, magnetic field angle is 5°, energy ratio 0.1 and impact duration 0.01 s: (*a*) temperature and melting layer (grey) of target; (*b*) maximum temperature of material.

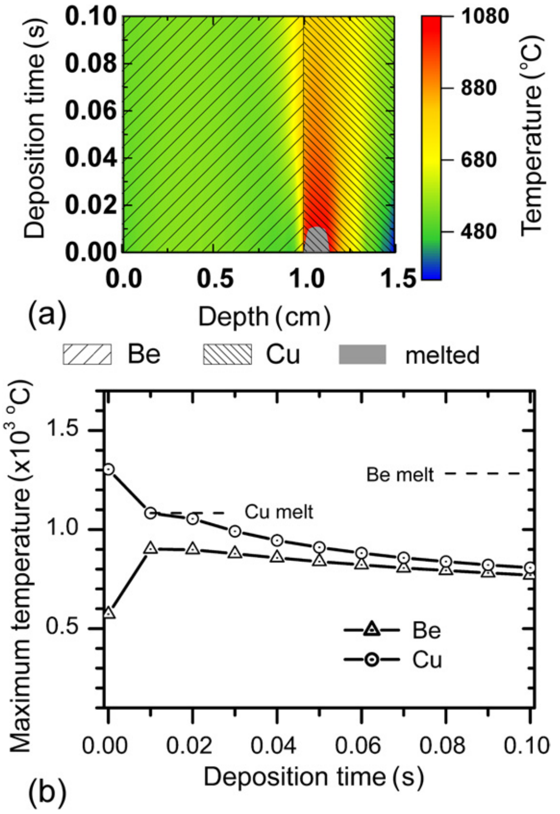

Figure 12. Thermal response as a function of the electron impact duration for Be armor directly at the normal axis above cooling tube. Electron energy, 50 MeV; energy ratio, 0.1 and magnetic field angle, 5°: (*a*) temperature and melting layer (grey) of target; (*b*) maximum temperature of material.

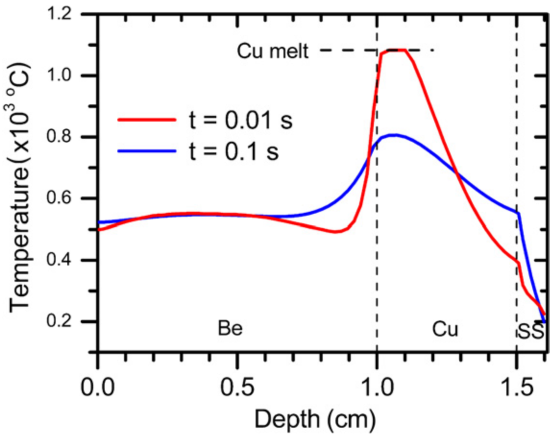

Figure 13. Temperature distribution as a result of runaway electron deposition along the normal axis above coolant tube for two extreme electron impact durations.

The heat conduction influence on the temperature rise of the materials is most notable during runaway electron impact of 0.1 s. Figure 12 shows that an energy deposition duration of electron impact that is longer than 0.01 s will cause more energy to be dissipated with the heat conduction process such that the copper layer will not melt. The heat load spatial distribution in armor and structural materials is shown in figure 13 for the two extreme cases of impact duration $t = 0.01$ s and $t = 0.1$ s.

To prevent melting of the heat sink and possible mitigation of the effect of runaway electrons, tungsten was analysed as an armor material. HEIGHTS calculations, however, show similar surface behaviour of the tungsten material thermal evolution as described above for beryllium (figure 14). Because tungsten is much heavier than beryllium the energy deposition distance for the runaway electrons is much shorter. Figure 14(*a*) shows the surface melting for different magnetic field inclinations, smaller for 5° because of deeper energy deposition (lower thermal load on surface layers). Similar processes take place for increasing particle energy (figure 14(*b*)). Deeper particle penetration decreases the thermal loading of the surface and the melted layer thickness is therefore lower. However, the negative aspect of using tungsten as an armor material is surface melting of tungsten by a wide range of runaway electron parameters. The heavy metal is a too efficient absorber of the runaway electron energy. Beryllium on the other hand, in opposite in this regard, i.e. it absorbs less electron energy and allows more electron energy to be deposited at the copper heat sink, and this can cause interlaminar damage.

Two solutions are proposed for this problem: increasing the beryllium thickness, or use of an additional ‘slowing down’ layer above the heat sink structure. Because beryllium is harder to use (being toxic, etc) the second option was analysed for the first wall heat protection. We studied an additional

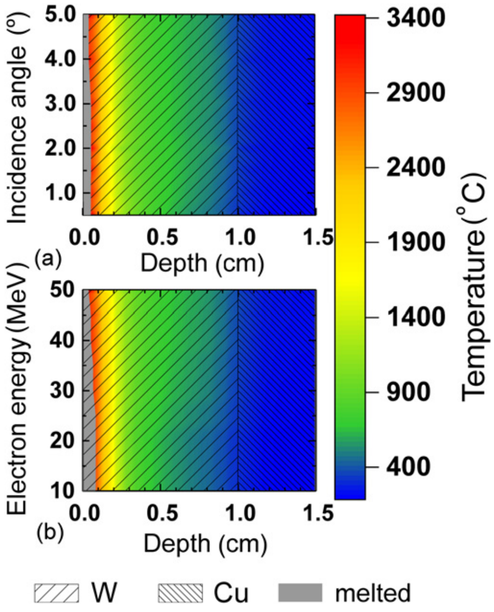

Figure 14. Temperature distribution after runaway electron deposition along the normal axis above coolant tube (energy ratio, 0.1; impact duration, 0.01 s) as dependence on: (*a*) magnetic field inclination angle of electron energy of 50 MeV; (*b*) runaway electron energy with magnetic field angle of 5°.

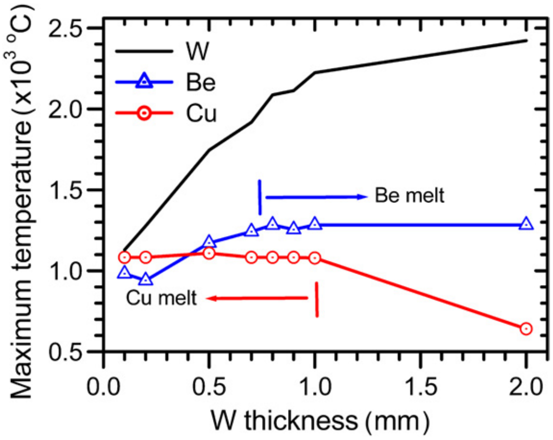

Figure 15. Dependence of maximum temperature on tungsten thickness located on copper surface. Incident electrons energy, 50 MeV; magnetic field angle, 5°, energy ratio, 0.1 and impact duration, 0.01 s.

tungsten layer (see thick dashed line in figure 6) above the copper heat think. The total size of the armor mockup is maintained constant, i.e. the beryllium layer was reduced in thickness and exchanged with an additional tungsten layer of equivalent thickness as shown with the dashed line in figure 6. Figure 15 shows the resulting HEIGHTS-computed runaway electron maximum temperature in all materials as a function of tungsten layer thickness, for the option where tungsten is located directly between beryllium and copper layers. This calculation is for the electron energy of 50 MeV, energy ratio of 0.1, magnetic field inclination of 5°, and impact duration of 0.01 s. Figure 15 also shows that copper surface begins to melt for a tungsten layer thinner than 1 mm and the beryllium layer melts for W thickness higher than 0.5 mm. This configuration therefore does not protect the structure from melting.

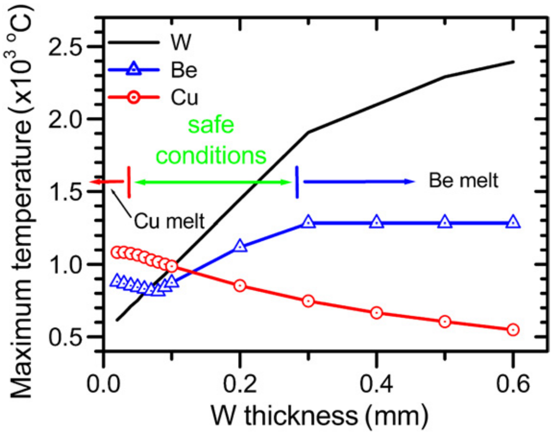

Figure 16. Dependence of maximum temperature on tungsten thickness located at 0.5 cm from the top surface of mockup (Sandwich design). Incident electrons energy, 50 MeV; magnetic field angle, 5°; energy ratio 0.1 and impact duration, 0.01 s.

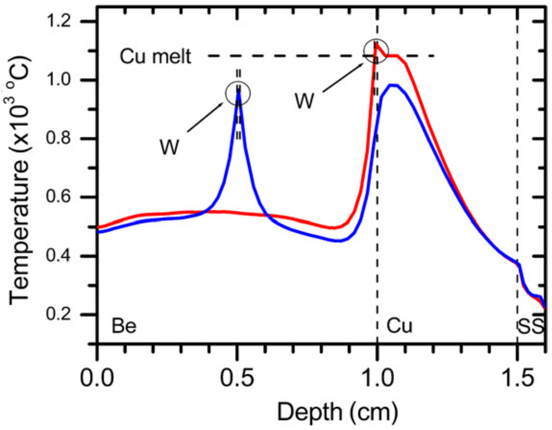

Figure 17. Temperature distribution as a result of runaway electron deposition along the normal axis above coolant tube for two extreme impact durations. The 0.1 mm W layer is located on the 5 mm depth (blue curve) and on the Cu surface (red curve). Incident electrons energy 50 MeV, magnetic field angle 5°, energy ratio 0.1, and impact duration 0.01 s.

However, opposite to the previous case, the location of the tungsten layer inside beryllium does make a difference in the structural response to the incident electrons. Figure 16 shows the maximum temperature in the materials for tungsten layer located at 0.5 cm from the top surface (at half-thickness of Be). Shown in green is the safe thickness of tungsten for which all layers will remain in solid state and no melting takes place. The explanation of this result can be found in figure 17. The temperature distribution is shown as a function of the mockup depth. Part of the deposited energy into copper is redistributed into the beryllium layer. The heat load spreads through all the mock up volume and the thermal heat wave is attenuated. The complex 'sandwich' design of the armor has the advantage of mitigating the heat load distributions in both the armor and in the structural materials. This design is complicated and requires careful manufacturing technology. However, current and advanced design technologies of fusion materials often explore various combinations of innovative bulk layers, composites and coatings [47, 48]. Optimization of first wall armor and structural materials design and configurations will be the subject of further future investigations using HEIGHTS integrated simulation package.

6. Conclusions

Physical and mathematical models are developed and benchmarked for simulating the main processes that occurs in ITER tokamak PFCs during runaway electron impact. Energy deposition, material thermal response and melting are calculated for a wide range of incident electron parameters: kinetic energy, magnetic field direction, energy ratio (along and across magnetic field direction), impact duration and armor material. Most previous calculations considered the initial runaway electron beam direction as parallel to the magnetic field flow. Our calculations showed that taking into account both the parallel and perpendicular electron energy components has a significant impact on the wall armor and structural thermal response. The actual incident angle of high-energy electrons varies in a narrow range because of their spiral trajectories and the small magnetic fields inclination angle. It is shown that the standard ITER geometry of first wall with beryllium armor can melt at the interface with the structural Cu material. Using tungsten armor instead caused surface melting of the mockup for all the parameters of runaway electrons considered in this study. Using an insert of a thin tungsten layer in between the beryllium armor and Cu structure prevents melting of all structure for the parameters considered. Design optimization using the HEIGHTS package can further improve and protect future tokamak devices from runaway electron damage.

Acknowledgments

This work is supplied by the US Department of Energy, Office of Fusion Energy Sciences.

References

[1] Einat M. and Jerby E. 1997 *Phys. Rev.* E **56** 5996
[2] Gill R.D., Alper B., Edwards A.W., Ingesson L.C., Johnson M.F. and Ward D.J. 2000 *Nucl. Fusion* **40** 163
[3] Chen Z.Y., Wan B.N., Lin S.Y., Shi Y.J. and Hu L.Q. 2006 *Phys. Lett.* A **351** 413
[4] Ninomiya H. *et al* 2000 *Nucl. Fusion* **40** 1287
[5] Nishimura E. 1983 *Japan. J. Appl. Phys.* **22** 1182
[6] Kurzan B., Steuer K.-H. and Fussmann G. 1995 *Phys. Rev. Lett.* **75** 4626
[7] Esposito B. *et al* 1996 *Plasma Phys. Control. Fusion* **38** 2035
[8] Tamai H., Yoshino R., Tokuda S., Kurita G., Neyatani Y., Bakhtiari M., Khayrutdinov R.R., Lukash V.E., Rosenbluth M.N. and JT-60 Team 2002 *Nucl. Fusion* **42** 290
[9] Shevelev A.E. *et al* 2004 *Plasma Phys. Rep.* **30** 159
[10] Martin-Solis J.R., Esposito B., Sanchez R., Poli F.M. and Panaccione L. 2006 *Phys. Rev. Lett.* **97** 165002
[11] Martın-Solıs J.R., Sanchez R. and Esposito B. 2000 *Phys. Plasmas* **7** 3369
[12] Pankratov I.M. 2000 *Problems At. Sci. Tech.* **6** 58
[13] Helander P., Eriksson L.-G. and Andersson F. 2002 *Plasma Phys. Control. Fusion* **44** B247
[14] Eriksson L.-G. and Helander P. 2003 *Comput. Phys. Commun.* **154** 175
[15] Gilligan J., Niemer K., Bourham M., Croessmann C., Hankins O., Tallavajula S., Mohanti R. and Orton N. 1990 *J. Nucl. Mater.* **176&177** 779
[16] Bartels H.-W. 1993 *Fusion Eng. Des.* **23** 323
[17] Kunugi T. 1993 *Fusion Eng. Des.* **23** 329
[18] Cardella A., Goren H., Lodato A., Ioki K. and Raffray R. 2000 *J. Nucl. Mater.* **283–287** 1105
[19] Maddaluno G., Maruccia G., Merola M. and Rollet S. 2003 *J. Nucl. Mater.* **313–316** 651
[20] Hender T.C. *et al* Progress in the ITER Physics Basis 2007 *Nucl. Fusion* **47** S128
[21] Hassanein A., Morozov V., Tolkach V., Sizyuk V. and Konkashbaev I. 2003 *Fusion Eng. Des.* **69** 781
[22] Hassanein A. and Konkashbaev I. 2003 *J. Nucl. Mater.* **313–316** 664
[23] Sizyuk V., Hassanein A. and Bakshi V. 2007 *J. Micro/Nanolithogr. MEMS MOEMS* **6** 043003
[24] Berestetskii V.B., Lifshitz E.M. and Pitaevskii L.P. 1982 Course in theoretical physics: V4. *Quantum Electrodynamics* 2nd edn (Burlington: Butterworth-Heinemann)
[25] Bazylev B., Miloshevsky G., Romanov G. and Suvorov A. 1994 Method Monte Carlo of the Bremsstrahlung modeling *Preprint* HMTI Minsk 97-103
[26] Miloshevskii G.V. 1998 *J. Eng. Phys. Thermophys.* **71** 874
[27] Bazylev B.N., Golub L.V., Romanov G.S. and Tolkach V.I. 1990 *J. Eng. Phys. Thermophys.* **58** 1012
[28] Bazylev B.N., Golub L.V., Romanov G.S. and Tolkach V.I. 1990 *J. Eng. Phys. Thermophys.* **59** 62
[29] Hubbell J.H., Gimm H.A. and Overbo I. 1980 *J. Phys. Chem. Ref. Data* **9** 1023
[30] Kadomtsev B.B. 1957 *JETP* **33** 151
[31] Halbleib J.A., Kensek R.P., Valdez G.D., Seltzer S.M. and Berger M.J. 1992 *IEEE Trans. Nucl. Sci.* **39** 1025
[32] Kolchuzhkin A.M. and Uchaikin V.V. 1978 *Introduction in Theory of Particles Transmission Through Matter* (Moscow: Amotizdat)
[33] Gluckstern R.L. and Hull M.H. 1953 *Phys. Rev.* **90** 1030
[34] Haug E. and Nakel W. 2004 *The Elementary Process of Bremsstrahlung* (*World Scientific Lecture Notes in Physics* vol 73) (Germany: Tubingen University) p 45
[35] Hammersley J.M. and Handscomb D.C. 1964 *Monte Carlo Methods* (London: Chapman and Hall)
[36] Plesheshnikov A.V. and Kolchuzhkin A.M. 1975 *At. Energy* **39** 53
[37] Hassanein A., Sizyuk V., Sizyuk T. and Morozov V. 2007 *Proc. SPIE* **6517** 65171X
[38] Hassanein A., Sizyuk V. and Sizyuk T. 2008 *Proc. SPIE* **6921** 692113
[39] Sizyuk V., Hassanein A., Morozov V., Tolkach V. and Sizyuk T. 2006 *Numer. Heat Transfer* A **49** 215
[40] Miloshevsky G.V., Sizyuk V.A., Partenskii M.B., Hassanein A. and Jordan P.C. 2006 *J. Comput. Phys.* **212** 25
[41] Lockwood G.J., Ruggles L.E., Miller G.H. and Halbleib J.A. 1980 Calorimetric measurement of electron energy deposition in extended media—theory versus experiment *Report* SAND79-0414 (Sandia Laboratories)
[42] Nakai Y. 1963 *Japan. J. Appl. Phys.* **2** 743
[43] Tabata A. 1994 *At. Data Nucl. Data Tables* (National Bureau of Standards, USA) **56** 105
[44] Spencer L.V. 1959 Energy dissipation by fast electrons *Monograph 1* (*Natl Bureau of Standards*)
[45] Kobetich E.J. and Katz R. 1968 *Phys. Rev.* **170** 391
[46] Morawska-Kaczynska M. and Huizenga H. 1992 *Phys. Med. Biol.* **37** 2103
[47] Gruber O. 2007 *Nucl. Fusion* **47** S622
[48] Shikov A.K. and Beliakov V.A. 2007 *J. Nucl. Mater.* **367–370** 1298